NANO EXPRESS

Morphology and Photoluminescence of HfO$_2$ Obtained by Microwave-Hydrothermal

**S. A. Eliziário · L. S. Cavalcante · J. C. Sczancoski ·
P. S. Pizani · J. A. Varela · J. W. M. Espinosa ·
E. Longo**

Abstract In this letter, we report on the obtention of hafnium oxide (HfO$_2$) nanostructures by the microwave-hydrothermal method. These nanostructures were analyzed by X-ray diffraction (XRD), field-emission gum scanning electron microscopy (FEG-SEM), transmission electron microscopy (TEM), energy dispersive X-ray spectrometry (EDXS), ultraviolet–visible (UV–vis) spectroscopy, and photoluminescence (PL) measurements. XRD patterns confirmed that this material crystallizes in a monoclinic structure. FEG-SEM and TEM micrographs indicated that the rice-like morphologies were formed due to an increase in the effective collisions between the nanoparticles during the MH processing. The EDXS spectrum was used to verify the chemical compositional of this oxide. UV–vis spectrum revealed that this material have an indirect optical band gap. When excited with 488 nm wavelength at room temperature, the HfO$_2$ nanostructures exhibited only one broad PL band with a maximum at around 548 nm (green emission).

Keywords HfO$_2$ · Nanoparticles · Morphology · Optical band gap · Photoluminescence

Introduction

Currently, the researches in *nanoscience* have been especially dedicated to the development of synthesis routes with ability for the formation of new nanostructured materials with distinct structural and morphological characteristics [1]. In principle, the chemical and physical properties of nanostructured oxide with well-defined morphologies are technologically more interesting because they differ from those in the bulk shape. For example, the porous CuO hollow structures as well as the Nb$_2$O$_5$ nanotubes are particularly attractive due to its applications in catalysis, Li$^+$ ion batteries and sensors [2–4].

In the last years, the hafnium oxide (HfO$_2$) has been extensively investigated as an alternative material to replace the silicon dioxide employed in gate dielectric systems of microelectronic devices [5–9]. Moreover, this material has a wide potential for the fabrication of complementary metal–oxide–silicon transistors with small dimensions and/or liquid crystals because of its high-K dielectric constant, relatively low leakage current, wide band gap (5.70 eV), good thermal stability, and high transparency [10–15]. Recently, different nano-sized particle materials (gold, cobalt, platinum, and germanium) have been embedded into the HfO$_2$ matrix to improve the interfacial and electrical properties of metal–oxide–semiconductor capacitors [16–19].

S. A. Eliziário · J. A. Varela · J. W. M. Espinosa · E. Longo
IQ-LIEC, Universidade Estadual Paulista, P.O. Box 355,
14801-907 Araraquara, SP, Brazil
e-mail: sayonara@iq.unesp.br

J. A. Varela
e-mail: varela@iq.unesp.br

J. W. M. Espinosa
e-mail: jose@liec.ufscar.br

E. Longo
e-mail: elson@iq.unesp.br

L. S. Cavalcante · J. C. Sczancoski (✉) · P. S. Pizani
LIEC, Departamento de Química e Física, Universidade Federal
de São Carlos, P.O. Box 676, 13565-905 São Carlos, SP, Brazil
e-mail: jcsfisica@gmail.com

L. S. Cavalcante
e-mail: laeciosc@bol.com.br

P. S. Pizani
e-mail: pizani@df.ufscar.br

The optical properties of pure or doped HfO_2 have been mainly focused on the photoluminescence, cathode-luminescence, and scintillation measurements [20–22]. For example, Rastorguev et al. [20] performed both photoluminescence and cathode-luminescence measurements on as-deposited HfO_2 films and on those heat treated at 800 °C for 30 min. The two broad PL bands detected in these films were attributed to the self-trapped excitons due to the presence of oxygen vacancies. Chang et al. [21] reported on the PL behavior of germanium nanocrystals embedded in HfO_2 and HfAlO structures. The differences observed between the PL spectra of these two samples were explained by the quantum confinement barrier. Taniguchi et al. [23] observed in Eu^{3+}-doped HfO_2 nanoparticles a broad photoluminescence (PL) band covering from ultraviolet to visible region of the electromagnetic spectrum as well as the characteristic transitions of Eu^{3+} ions. According to these authors, the broad PL band originates from electron-hole recombination via surface defect centers. Also, Ni et al. [24] described that the PL emissions of HfO_2 films are controlled by the concentration of oxygen vacancies into the lattice.

In terms of structural characteristics, the HfO_2 presents a monoclinic structure with space group $P2_1/c$ in the range from room temperature up to 1,700 °C [25, 26]. The increase of temperature up to 2,600 °C promotes a phase transition from monoclinic ($P2_1/c$) to tetragonal structure ($P4_2/nmc$), reducing the unit cell volume to approximately 3.5% [27, 28]. Above 2,600 °C, this compound exhibits a fluorite-type cubic structure with space group $Fm\overline{3}m$ [28]. According to the literature [29, 30], this high temperature cubic phase can be stabilized at room temperature doping the HfO_2 lattice with Y^{3+} ions.

The literature has reported the preparation of pure or doped HfO_2 (nanoparticles, powders, or films) by different synthetic routes, mainly including: alkoxide in solvents non-aqueous [31], non-hydrolytic sol–gel [32], solvent casting with oxo-clusters [33], non-aqueous sol–gel with atomic layer deposition [34], conventional hydrothermal (CH) [35–37], ultrasonically assisted hydrothermal [38], pulsed laser deposition [39], plasma-assisted chemical vapor deposition [40], and solvothermal [41, 42]. In particular, the CH is an interesting synthesis method due to the formation of different oxides with a good control on the morphology and particle sizes, high degree of crystallinity, and easy dispersion in aqueous medium [43]. Although this method can be efficient in the preparation of materials using low heat treatment temperatures, its main drawback is related to the long processing times. In order to overcome this problem, Komarneni and Katsuki [44] innovated the CH systems through the use of microwave radiation. The development of this new system, known as microwave-hydrothermal (MH) [45, 46], promoted an increase in the kinetics of crystallization by 1 or 2 orders of magnitude, drastically reducing the processing times for minutes or some hours during the synthesis. These advantages are arising from the direct interaction between the microwave-radiation with the atoms, ions, and/or molecules of the aqueous medium and/or dispersed phase [47]. In this case, this interaction induces a molecular rotation because of the permanent or induced dipole alignment with the oscillating microwave electric field (frequency of 2.45 GHz) [48]. This phenomenon promotes a transformation from rotational energy to heat, which is necessary for the formation and crystallization of the particles. Therefore, in this letter, we report on the obtention of rice-like HfO_2 nanostructures by the MH method.
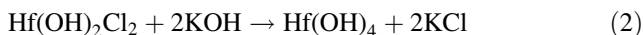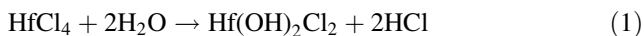
The structural and morphological properties were characterized by means of X-ray diffraction (XRD), field-emission gun scanning electron microscopy (FEG-SEM), transmission electron microscopy (TEM), and energy dispersive X-ray spectrometry (EDXS). The optical properties were analyzed through ultraviolet–visible (UV–vis) absorption spectroscopy and photoluminescence (PL) measurements.

Experimental Details

Synthesis and Reactions of Rice-like HfO_2 Nanostructures

The rice-like HfO_2 nanostructures were obtained by the MH method. More details on this equipment have been reported in Ref. [49]. The typical experimental procedure is described as follows: 5×10^{-3} mol of hafnium chloride ($HfCl_4$) [99.9% purity, Sigma-Aldrich] were dissolved in 100 mL of deionized water heated at 80 °C. In this first stage, the hydration reaction takes place by means of the interaction between the water molecules with the $HfCl_4$ [50], leading to the formation of hafnium hydroxichlorides ($Hf(OH)_2Cl_2$) and chloridric acid (HCl) (Eq. 1). In the second stage, the solution pH was adjusted up to 14 by the addition of potassium hydroxide (KOH) (2 mol/L) [99.5% purity, Merck]. In this case, the chemical reaction between $Hf(OH)_2Cl_2$ and KOH resulted in the formation of hafnium hydroxide [51] (Eq. 2). In the sequence, the solution was transferred into a Teflon autoclave, which was sealed and placed inside the MH system (2.45 GHz, maximum power of 800 W). The MH conditions were performed at 140 °C for 1 h. The heating rate in this system was fixed at 10 °C/min and the pressure into the autoclave was stabilized at 294 kPa. Thus, the heating promoted by the microwave radiation accelerated the dehydration reaction of $Hf(OH)_4$, forming the HfO_2 precipitates into the aqueous medium (Eq. 3). After MH processing, this resultant solution was washed with deionized water several times to neutralize the

solution pH (≈ 7). Finally, the white precipitates were collected and dried at room temperature.

$$HfCl_4 + 2H_2O \rightarrow Hf(OH)_2Cl_2 + 2HCl \quad (1)$$

$$Hf(OH)_2Cl_2 + 2KOH \rightarrow Hf(OH)_4 + 2KCl \quad (2)$$

$$Hf(OH)_4 \rightarrow HfO_2 + 2H_2O. \quad (3)$$

Characterization of Rice-like HfO_2 Nanostructures

The rice-like HfO_2 nanostructures were structurally characterized by X-ray powder diffraction (XRD) using a Rigaku-DMax/2500PC (Japan) with Cu–Kα radiation ($\lambda = 1.5406$ Å) in the 2θ range from 20° to 80° with scanning rate of 0.02°/min. The morphologies were investigated through a FEG-SEM (Supra 35-VP, Carl Zeiss, Germany) operated at 6 keV and with a TECNAI G2 TEM (FEI Corporation, Holland) operated at 200 keV. UV–vis spectra were taken using a Cary 5G (Varian, USA) spectrophotometer in diffuse reflection mode. PL measurements were performed using a U1000 (Jobin-Yvon, France) double monochromator coupled to a cooled GaAs photomultiplier with a conventional photon counting system. An argon ion laser ($\lambda = 488$ nm) was used as excitation source, keeping its maximum output power at 25 mW. UV–vis and PL spectra were taken three times for each sample to ensure the reliability of the measurements. All measurements were performed at room temperature.

Results and Discussion

X-ray Diffraction Analysis

Figure 1 shows the XRD patterns of rice-like HfO_2 nanostructures obtained by MH at 140 °C for 1 h.

All diffraction peaks were indexed to the monoclinic structure with space group $P2_1/c$ in agreement with the respective Joint Committee on Powder Diffraction Standards (JCPDS) No. 34-0104 [52]. The broadening of these peaks implies that the obtained samples are composed by nanoscale structures. No secondary peaks were observed, indicating the high purity of the samples after MH processing. The data on the position and full width at half height of all diffraction peaks were used in the DBWS program [53] to estimate the lattice parameter values and unit cell volume. The obtained results were compared with those previously reported in the literature, as shown in Table 1.

As it can be seen in this table, the lattice parameters obtained in this work are very close to the reported in the literature [54–56]. However, the small differences observed between these values can be related to the synthesis methods. Therefore, we believe that the experimental
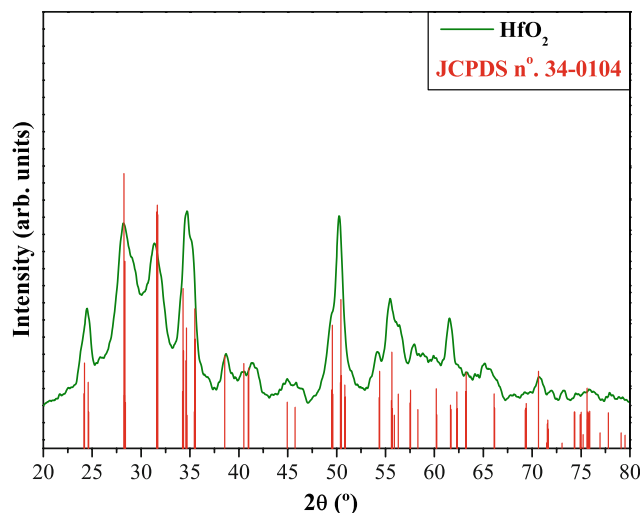

Fig. 1 XRD pattern of rice-like HfO_2 nanostructures obtained by MH at 140 °C for 1 h. The vertical lines indicate the position and relative intensity of JCPDS card no. 35-0104

conditions (heat treatment temperature, heating rate, and/or processing time) employed in the synthesis methods to obtain the HfO_2 (film or powder) are able to promote the formation of particles with several morphologies and different sizes, probably inducing residual stresses, and/or distortions into the lattice [57].

Schematic Representation for the HfO_2 Unit Cell

Figure 2 shows the schematic representation of monoclinic HfO_2 unit cell ($1 \times 1 \times 1$) with space group $P2_1/c$.

This unit cell was modeled through the Java Structure Viewer (version 1.08lite for Windows) and VRML-View (version 3.0 for Windows) (http://www.jcrystal.com/steen weber/JAVA/JSV/jsv.html, http://www.km.kongsberg.com/sim) programs, using the atomic coordinates listed in Table 2 [58]. In this monoclinic structure, the hafnium atoms are bonded to six oxygen atoms, forming [HfO_6] clusters with octahedral coordination. Moreover, these octahedral clusters are distorted because the different bond angles and/or distances between the O–Hf–O bonds [59].

### FEG-SEM and TEM Analyses of Rice-like HfO_2 Nanostructures

Figure 3 shows the FEG-SEM, TEM, HR-TEM micrographs, and EDXS spectra of rice-like HfO_2 nanostructures obtained by MH at 140 °C for 1 h.

FEG-SEM micrograph indicated the presence of several rice-like HfO_2 nanostructures with agglomerate and polydisperse nature (Fig. 3a). The high magnification FEG-SEM micrographs showed that these morphologies are composed of several primary particles (Fig. 3b, c). In fact,

Table 1 Atomic coordinates used to model the HfO$_2$ unit cell

Method	T (°C)	Time (h)	Lattice parameter (Å)			Unit cell volume (Å^3)	Ref. [ ]
			a	b	c		
ALD	–	–	5.1	5.2	5.3	140.556	[54]
PIAD	550	3	5.09	5.15	5.24	137.358(7)	[55]
LDA	–	–	5.106	5.165	5.281	139.273(1)	[56]
MH	140	1	5.160(2)	5.179(2)	5.311(1)	66.528(5)	[✠]
JCPDS			5.285(1)	5.181(9)	5.115(7)	140.102(9)	[52]

T temperature, t time, $Ref.$ references, $PIAD$ Plasma ion assisted deposition, ALD atomic layer deposition, LDA local-density approximation, and [✠] This work
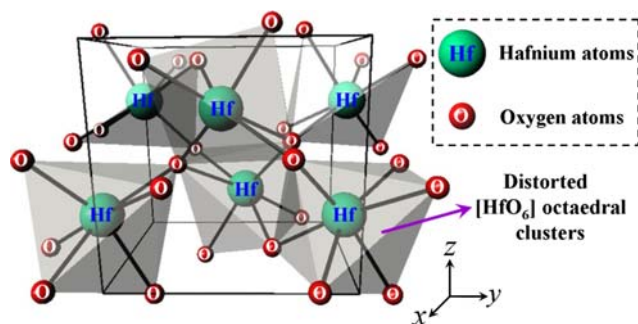
Fig. 2 Schematic representation of HfO$_2$ unit cell (1 × 1 × 1) illustrating the distorted [HfO$_6$] clusters

Table 2 Comparative results between the optical band gap energy of rice-like HfO$_2$ nanostructures obtained in this work with those reported in the literature by other methods

Atom	Site	x	y	z
Hafnium	4e	0.2755	0.0397	0.2080
Oxygen	4e	0.0742	0.3316	0.3467
Oxygen	4e	0.4487	0.7581	0.4801

$a = 5.160(2)$ Å, $b = 5.179(2)$ Å, $c = 5.311(1)$ Å, $\alpha = \gamma = 90°$ and $\beta = 99.04247°$

probably the Brownian motion of these particles in suspension resulted in collision events between them [60]. Hence, we believe that the microwave radiation intensified the effective collision rates of the primary particles. In principle, when two nanoparticles collide with the same crystallographic orientation, the adhesion process occurs with highest probability. This probability is slightly reduced when the nanoparticles are not aligned. After this phenomenon, the nanoparticles remain in contact by Van der Waals forces and the coalescence process takes place, resulting in the formation of rice-like morphologies. This conclusion can be confirmed by means of low magnification TEM micrographs in Fig. 3d and e, where it was verified that these morphologies are formed by several

aggregated nanoparticles. Also, in these micrographs, the bright areas correspond to the individual nanoparticles, while the black areas indicate the regions with stacking between the nanoparticles oriented in different crystallographic planes. The EDXS analysis revealed that the nanoparticles are chemically composed of Hf and O atoms. Therefore, this result suggests that the MH conditions performed at 140 °C for 1 h lead to the formation of pure HfO$_2$ phase (Inset in Fig. 3e). The presence of Cu atoms in the spectrum is arising from the carbon-coated copper grids. Figure 3f shows a high magnification TEM micrograph of an individual HfO$_2$ nanoparticle chosen in Fig. 3e (black rectangle). On this selected region, it was performed a HR-TEM micrograph as well as a Fourier-transform. In the Fourier-transform, the respective crystallographic planes were estimated by the FTL-SE program (version 1.10 for Windows) (http://www.jcrystal.com/jcrystal.html). The interplanar spacing was determined in approximately 3.12 Å by means of the HR-TEM micrograph, which correspond to the ($\bar{1}$11) crystallographic plane. The Fourier-transform confirmed that these morphologies present a single phase with monoclinic structure. According to Debye scattering equation described in the literature [42, 61], the preferential growth direction of these morphologies occurs along the [100] direction.

Recently, Mohanty and Landskron [62] observed this same morphology in periodic mesoporous organosilica synthesized by the template assisted sol–gel method using a chain-type precursor. According to these authors, this morphology is a kind of mesostructure formed by periodic one-dimensional channels, containing pore sizes of ca. 4 nm and channel wall diameters of ca. 6 nm.

Particle Size Distribution (Height and Width) of Rice-like HfO$_2$ Nanostructures

FEG-SEM and TEM micrographs were also employed to evaluate the average particle size distribution (height and width) of rice-like HfO$_2$ nanostructures through the measures of approximately 100 nanostructures (Fig. 4a, b).

Fig. 3 **a** Low magnification FEG-SEM micrograph of several rice-like HfO$_2$ nanostructures obtained by MH at 140 °C for 1 h; **b, c** High magnification FEG-SEM micrographs of a group of rice-like nanostructures; **d, e** Low magnification TEM micrographs of aggregated HfO$_2$ nanostructures; Inset in (**e**) shows the EDXS spectrum of HfO$_2$ nanostructures; and **f** HR-TEM micrograph of an individual nanoparticle selected in (**e**) (*black rectangle*). Inset in (**f**) show the corresponding Fourier-transform obtained on this region
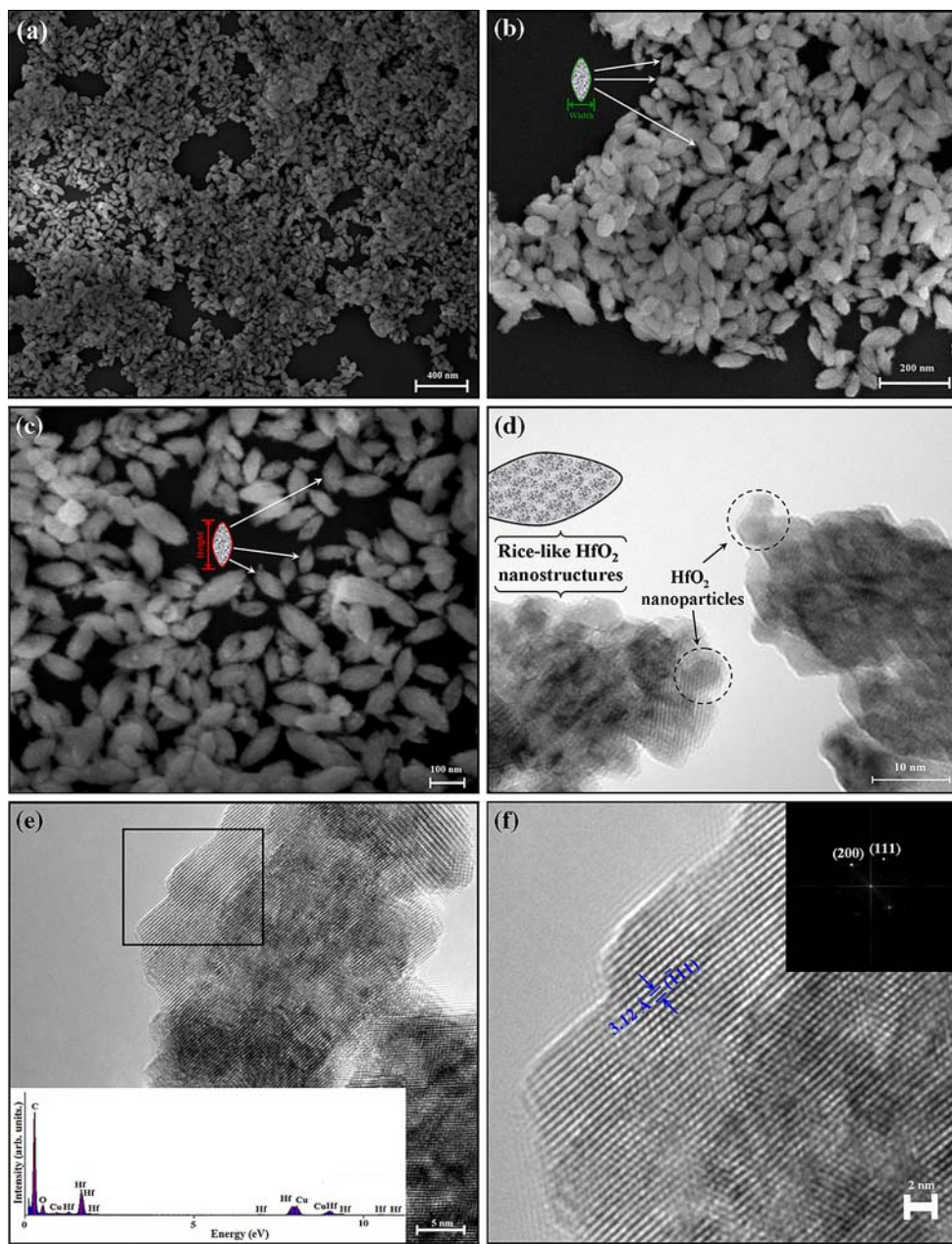
As it was verified in the FEG-SEM micrographs (Fig. 3a–c), the rice-like HfO$_2$ nanostructures exhibited a polydisperse particle size distribution (height and width). Therefore, the best fit for this system is a lognormal function, which is described by the following equation:

$$y = y_0 + \frac{A}{\sqrt{2\pi}wx}e^{\frac{-[\ln\frac{x}{x_c}]^2}{2w^2}}, \qquad (4)$$

where y_0 is the first value in y-axis, A is the amplitude, w is the width, π is a constant, x_c is the center value of the distribution curve in x-axis. Thus, the distribution is asymmetrical on the logarithmic scale of average particle size [63, 64]. Figure 4a shows the average particle width distribution in the range from 15 to 75 nm for the rice-like HfO$_2$ nanostructures. In this case, it was noted that approximately 81% particles presented an average width between 35 and 55 nm. On the other hand, approximately 77% particles exhibited an average height in the range from 85 to 105 nm. Possibly, the differences observed between width and height is caused by the increase in the effective collision rates between the nanoparticles by the microwave radiation, as previously described in the text.
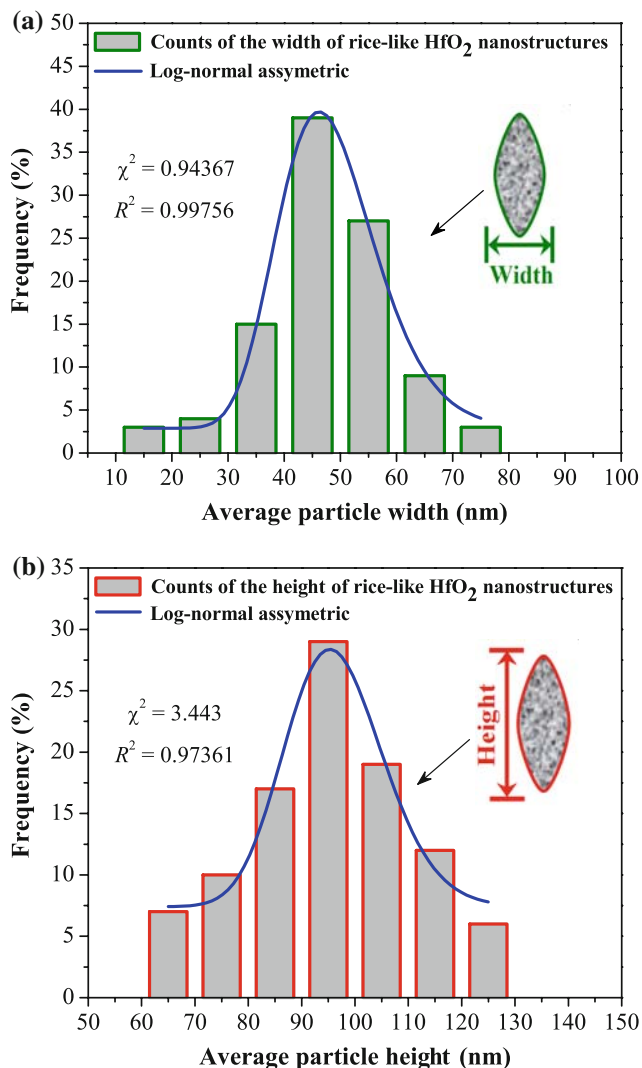
Fig. 4 Average particle height and width distributions of rice-like HfO$_2$ nanostructures obtained by MH at 140 °C for 1 h

Fig. 5 **a** UV–vis absorbance spectra of rice-like HfO$_2$ nanostructures obtained by MH at 140 °C for 1 h. Inset illustrates a wide band model composed of intermediary levels within the band gap as well as the indirect electronic transition process. **b** PL spectrum at room temperature of rice-like HfO$_2$ nanostructures. Inset shows the different bond angles between the O–H–O bonds for the [HfO$_6$] clusters

Ultraviolet–Visible Absorption Spectroscopy and Photoluminescence Analyses

Figure 5a and b shows the UV–vis and PL spectra of rice-like HfO$_2$ nanostructures obtained by MH at 140 °C for 1 h, respectively.

The optical band gap energy (E_{gap}) was estimated by the method proposed by Wood and Tauc [65]. According to these authors, the E_{gap} is associated with absorbance and photon energy by the following equation:

$$h\nu\alpha \propto (h\nu - E_{gap})^n, \tag{5}$$

where α is the absorbance, h is the Planck constant, ν is the frequency, E_{gap} is the optical band gap, and n is a constant associated to the different electronic transitions ($n = \frac{1}{2}$, 2, $\frac{3}{2}$ or 3 for direct allowed, indirect allowed, direct forbidden,
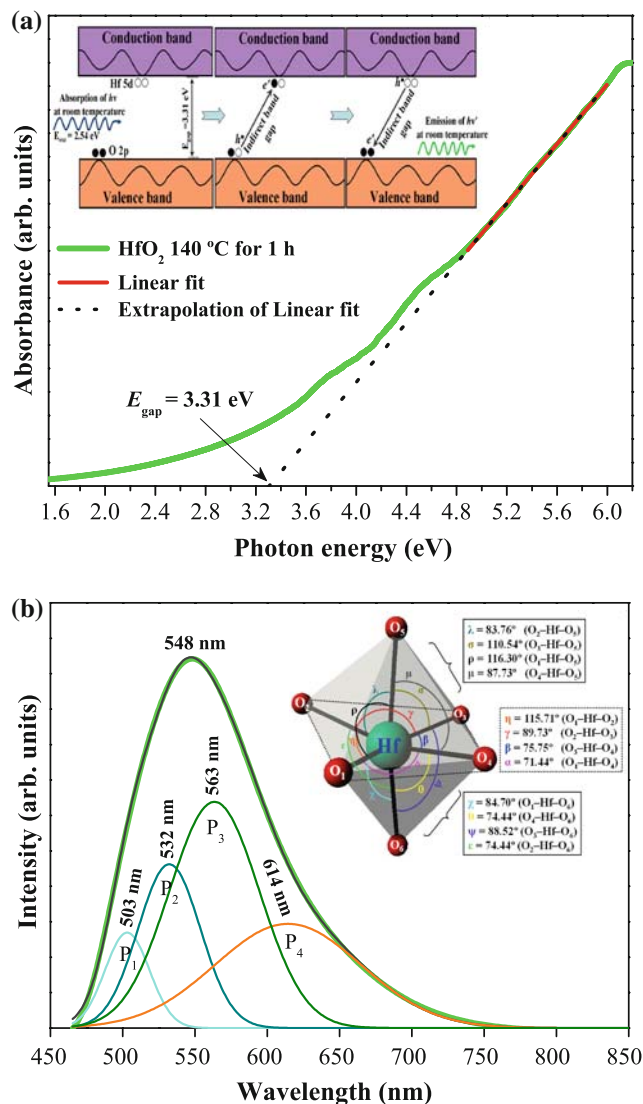
and indirect forbidden transitions, respectively). According to Park et al. [66] and Ramo et al. [67] the monoclinic HfO$_2$ structure presents an indirect band gap. In principle, the band gap energy is considered indirect when the electronic transition occurs from maximum-energy states near or in the valence band to minimum-energy states below or in the conduction band, but in different regions in the Brillouin zone [68] (Inset in Fig. 5b). Based on these information, the E_{gap} of HfO$_2$ nanoparticles was calculated using $n = 2$ in Eq. 5 and extrapolating the linear portion of the curve or tail. The obtained result indicated an E_{gap}

Table 3 Results obtained by the deconvolution of the PL spectrum of rice-like HfO_2 nanoparticles formed by MH at 140 °C for 1 h

P_1 Peak		P_2 Peak		P_3 Peak		P_4 Peak	
Center (nm)	Area (%)	Center (nm)	Area (%)	Center (nm)	Area (%)	Center (nm)	Area (%)
503	8.50	532	20.40	563	40.66	614	30.44

value at around 3.31 eV (Fig. 5a), which is lower than those reported in the literature by means of experimental methods or theoretical calculations [69–72]. A plausible explication for this phenomenon can be the existence of several intermediary energy levels within the band gap, as consequence of the symmetry break (oxygen vacancies) and/or distortions on the $[HfO_6]$ clusters because the influence of microwave radiation. It is possible that these energy levels are basically composed of oxygen 2p states (near the valence band) and hafnium 5d states (below the conduction band) [73].

The PL spectrum of rice-like HfO_2 nanostructures shows a broad band covering a large part of the visible spectrum with a maximum situated at 548 nm (green emission). This PL profile suggests an emission mechanism characterized by the participation of several energy levels or light emission centers able to trap electrons within the band gap. Hence, it was performed the deconvolution of the PL spectrum to qualitatively estimate the contribution of each individual component in the emission process. The deconvolution was performed trough the PeakFit program (4.05 version) using the Voigt area function (http://www.sigmaplot.com/products/peakfit/). The deconvolution results showed that the PL spectrum was better adjusted by four components. The P_1 peak located at 503 nm is responsible for the cyan emission component. The P_2 and P_3 peaks situated at 532 and 563 nm correspond to the green light centers, respectively. The P_4 peak located at 614 nm is ascribed to the orange light center. The obtained deconvolution results are displayed in Table 3.

In this table, it was observed that the smallest area is associated to the cyan light emission component (P_1 peak). Therefore, this result suggests that there is a lower contribution of the shallow holes for the PL spectrum. On the other hand, the green and orange light components (P_1, P_2, P_3, and P_4) are related to the deep holes, which are predominant in the PL behavior.

In the last years, investigations performed through the electron paramagnetic resonance (EPR) technique in HfO_2 bulk have shown the existence of Hf^{3+} defects into the structure, acting as charge trapping centers. These defects were detected near or on the HfO_2 surface, suggesting that they are a kind of oxygen vacancy [74]. Although the oxygen vacancies can be considered key factors in the PL behavior of HfO_2, possibly in our case, the distortions on

the $[HfO_6]$ clusters caused by the interaction with the microwave radiation contributed for the formation of intermediary energy levels (deep and shallow holes) within the band gap. On the basis of this hypothesis, inset in Fig. 5b shows 12 different bond angles values for the $[HfO_6]$ clusters. The bond angles were qualitatively estimated by the Java Structure Viewer program (http://www.jcrystal.com/steenweber/JAVA/JSV/jsv.html), considering the crystallographic data displayed in Table 2. In principle, future investigations based on both experimental data and theoretical calculations will be necessary to a better understanding on the intermediary energy level distribution and nature of the structural defects as well as provide information on its origins within the band gap of HfO_2.

Conclusions

In summary, rice-like HfO_2 nanostructures were obtained by the MH method at 140 °C for 1 h. XRD patterns revealed that this oxide crystallizes in a monoclinic structure with space group $P2_1/c$ without the presence of secondary phases. FEG-SEM and TEM micrographs indicated that the MH processing favored the formation of rice-like HfO_2 nanostructures with agglomerate and polydisperse nature. These morphological characteristics were attributed to the effective collision rates between the primary particles by the microwave radiation and due to its mutual interactions by Van der Waals forces. These nanostructures exhibited an average width in the range from 15 to 75 nm as well as an average height between 85 and 105 nm. The UV–vis absorption spectrum showed an E_{gap} value of 3.31 eV, which was ascribed to the presence of intermediary energy levels between the valence band and conduction bands (deep and shallow holes) within the band gap. The PL behavior was related to the existence of oxygen vacancies and/or distortions on the $[HfO_6]$ clusters into the lattice.

References

1. J. Liu, F. Liu, K. Gao, J. Wu, D. Xue, J. Mater. Chem. (2009). doi:10.1039/b900116f
2. C. Yan, D. Xue, Adv. Mater. **20**, 1055 (2008)
3. J. Liu, D. Xue, Adv. Mater. **20**, 2622 (2008)
4. C. Yan, J. Liu, F. Liu, J. Wu, K. Gao, D. Xue, Nanoscale Res. Lett. **3**, 473 (2008)
5. C. Sargentis, K. Giannakopoulos, A. Travlos, D. Tsamakis, Physica E **38**, 85 (2007)
6. Y.T. Chen, H. Zhao, J.H. Yum, Y. Wang, J.C. Lee, Appl. Phys. Lett. **94**, 213505 (2009)
7. G. Chakrabortya, C.K. Sarkar, J. Appl. Phys. **104**, 034313 (2008)
8. C. Sargentis, K. Giannakopoulos, A. Travlos, D. Tsamakis, Surf. Sci. **601**, 2859 (2007)
9. J.S. Lee, J. Cho, C. Lee, I. Kim, J. Park, Y.M. Kim, H. Shin, J. Lee, F. Caruso, Nat. Nanotechnol. **2**, 790 (2007)
10. M. Modreanu, J. Sancho-Parramon, D. O'Connella, J. Justice, O. Durand, B. Servet, Mater. Sci. Eng. B **118**, 127 (2005)
11. J.J. Lee, X. Wang, W. Bai, N. Lu, D.L. Kwong, IEEE Trans. Electron Devices **5**, 2067 (2003)
12. W.K. Lee, B.Y. Oh, J.H. Lim, H.G. Park, B.Y. Kim, H.J. Na, D.S. Seoa, Appl. Phys. Lett. **94**, 223507 (2009)
13. E. Rauwel, M.G. Willinger, F. Ducroquet, P. Rauwel, I. Matko, D. Kiselev, N. Pinna, J. Phys. Chem. C **112**, 12754 (2008)
14. C. LeLuyer, M. Villanueva-Ibañez, A. Pillonnet, C. Dujardin, J. Phys. Chem. A **112**, 10152 (2008)
15. A.B. Lebedev, S.A. Pul'nev, V.V. Vetrov, Y.A. Burenkov, Phys. Solid State **40**, 1155 (1998)
16. J.Y. Yang, J.H. Kim, W.J. Choi, Y.H. Do, C.O. Kim, J.P. Hong, J. Appl. Phys. **100**, 066102 (2006)
17. C. Lee, J.H. Kwon, J.S. Lee, Y.M. Kim, Y. Choi, H. Shin, J. Lee, Appl. Phys. Lett. **91**, 153506 (2007)
18. C. Sargentis, K. Giannakopoulos, A. Travlos, N. Boukos, D. Tsamakis, Appl. Phys. Lett. **88**, 073106 (2006)
19. W.A. Winkenwerder, J.G. Ekerdt, J. Cryst. Growth **310**, 3758 (2008)
20. A.A. Rastorguev, V.I. Belyi, T.P. Smirnova, L.V. Yakovkina, M.V. Zamoryanskaya, V.A. Gritsenko, H. Wong, Phys. Rev. B **76**, 235315 (2007)
21. S.T. Chang, S.H. Liao, J. Vac. Sci. Technol. B **27**, 535 (2009)
22. S. Kim, S.W. Hwang, S.H. Choi, R.G. Elliman, Y.M. Kim, Y.J. Kim, J. Appl. Phys. **105**, 106112 (2009)
23. T. Taniguchi, N. Sakamoto, T. Watanabe, N. Matsushita, M. Yoshimura, J. Phys. Chem. C **112**, 4884 (2008)
24. J. Ni, Q. Zhou, Z. Li, Z. Zhang, Appl. Phys. Lett. **93**, 011905 (2008)
25. C. Wang, M. Zinkevichw, F. Aldinger, J. Am. Ceram. Soc. **89**, 3751 (2006)
26. J. Wang, H.P. Li, R. Stevens, J. Mater. Sci. **27**, 1992 (1992)
27. C.H. Lu, J.M. Raitano, S. Khalid, L. Zhang, S.W. Chan, J. Appl. Phys. **103**, 124303 (2008)
28. F. Cardarelli, *Materials Handbook: A Concise Desktop Reference*, 2nd edn. (Springer-Verlag, New York, 2008)
29. T.A. Lee, A. Navrotsky, J. Mater. Res. **19**, 1855 (2004)
30. A. Lakhlifi, Ch. Leroux, P. Satre, B. Durand, M. Roubin, G. Nihoul, J. Solid State Chem. **119**, 289 (1995)
31. L. Armelao, H. Bertagnolli, D. Bleiner, M. Groenewolt, S. Gross, V. Krishnan, C. Sada, U. Schubert, E. Tondello, A. Zattin, Adv. Funct. Mater. **17**, 1671 (2007)
32. E. Tirosh, G. Markovich, Adv. Mater. **19**, 2608 (2007)
33. M. Vittadello, E. Negro, S. Lavina, G. Pace, A. Safari, V. Di Noto, J. Phys. Chem. B **112**, 16590 (2008)
34. E. Rauwel, M.G. Willinger, F. Ducroquet, P. Rauwel, I. Matko, D. Kiselev, N. Pinna, J. Phys. Chem. C **112**, 12754 (2008)
35. H. Toraya, M. Yoshimura, S. Somiya, J. Am. Ceram. Soc. **65**, c159 (2006)
36. G. Stefanic, S. Music, K. Molcanov, J. Alloys Compd. **387**, 300 (2005)
37. G. Stefanic, K. Molcanov, S. Music, Mat. Chem. Phys. **90**, 344 (2005)
38. P.E. Meskin, F.Y. Sharikov, V.K. Ivanov, B.R. Churagulov, Y.D. Tretyakov, Mater. Chem. Phys. **104**, 439 (2007)
39. J.Z. Wang, Z.Q. Shi, Y. Shi, L. Pu, L.J. Pan, R. Zhang, Y.D. Zheng, Z.S. Tao, F. Lu, Appl. Phys. A **94**, 399 (2009)
40. G. Lucovsky, K.B. Chung, J.W. Kim, D. Norlund, Microelectron. Eng. **86**, 1676 (2009)
41. M. Niederberger, G. Garnweitner, N. Pinna, G. Neri, Prog. Solid State Chem. **33**, 59 (2005)
42. N. Pinna, G. Garnweitner, M. Antonietti, M. Niederberger, Adv. Mater. **16**, 2196 (2004)
43. S. Komarneni, R. Roy, Q.H. Li, Mater. Res. Bull. **27**, 1393 (1992)
44. S. Komarneni, H. Katsuki, Pure Appl. Chem. **74**, 1537 (2002)
45. S. Komarneni, R.K. Rajha, H. Katsuki, Mater. Chem. Phys. **61**, 50 (1998)
46. L.S. Cavalcante, J.C. Sczancoski, L.F. Lima Jr., J.W.M. Espinosa, P.S. Pizani, J.A. Varela, E. Longo, Cryst. Growth Des. **9**, 1002 (2009)
47. T. Thongtem, A. Phuruangrat, S. Thongtem, Curr. Appl. Phys. **8**, 189 (2008)
48. T. Thongtem, A. Phuruangrat, S. Thongtem, Appl. Surf. Sci. **254**, 7581 (2008)
49. J.C. Sczancoski, L.S. Cavalcante, M.R. Joya, J.W.M. Espinosa, P.S. Pizani, J.A. Varela, E. Longo, J. Colloid Interface Sci. **330**, 227 (2009)
50. E. Barraud, S. Bégin-Colina, G.L. Caërc, F. Villieras, O. Barres, J. Solid State Chem. **179**, 1842 (2006)
51. V.P. Vasilev, A.I. Lytkin, N.V. Chernyavskaya, J. Therm. Anal. Calorim. **55**, 1003 (1999)
52. Joint Committee on Powder Diffraction Standards. Diffraction Data File, n°. 34-0104, International Centre for Diffraction Data (ICSD, formerly JCPDS), Newtown Square, PA (2001)
53. R.A. Young, A. Sakthivel, T.S. Moss, C.O. Paiva-Santos, J. Appl. Cryst. **28**, 366 (1995)
54. J.C. Kim, J.S. Heo, Y.S. Cho, S.H. Moon, Thin Solid Films **517**, 5695 (2009)
55. M. Modreanu, J. Sancho-Parramon, D. O'Connella, J. Justice, O. Durand, B. Servet, Mater. Sci. Eng. B **118**, 127 (2005)
56. X. Zhao, D. Vanderbilt, Phys. Rev. B **65**, 233106 (2002)
57. J.C. Sczancoski, M.D.R. Bomio, L.S. Cavalcante, M.R. Joya, P.S. Pizani, J.A. Varela, E. Longo, M.S. Li, J.A. Andrés, J. Phys. Chem. C **113**, 5812 (2009)
58. R.E. Hann, P.R. Suitch, J.L. Pentecost, J. Am. Ceram. Soc. **68**, 285 (1985)
59. C.H. Chen, H.L. Hwang, F.C. Chiu, J. Appl. Phys. **105**, 103910 (2009)
60. E.J.H. Lee, C. Ribeiro, E. Longo, E.R. Leite, Chem. Phys. **328**, 229 (2006)
61. N. Pinna, Progr. Colloid Polym. Sci. **130**, 29 (2005)
62. P. Mohanty, K. Landskron, Nanoscale Res. Lett. **4**, 169 (2009)
63. P.K. Swamee, J. Hydrol. Eng. **7**, 441 (2002)
64. R.R. Irani, J. Phys. Chem. **63**, 1603 (1959)
65. D.L. Wood, J. Tauc, Phys. Rev. B **5**, 3144 (1972)
66. J.W. Park, D.K. Lee, D. Lim, H. Lee, S.H. Choi, J. Appl. Phys. **104**, 033521 (2008)
67. D.M. Ramo, J.L. Gavartin, A.L. Shluger, Phys. Rev. B **75**, 205336 (2007)
68. L.S. Cavalcante, M.F.C. Gurgel, E.C. Paris, A.Z. Simões, M.R. Joya, J.A. Varela, P.S. Pizani, E. Longo, Acta Mater. **55**, 6416 (2007)

69. J.L. Gavartin, D.M. Ramo, A.L. Shluger, G. Bersuker, B.H. Lee, Appl. Phys. Lett. **89**, 082908 (2006)
70. E.A. Choi, K.J. Chang, Appl. Phys. Lett. **94**, 122901 (2009)
71. E.E. Hoppe, R.S. Sorbello, C.R. Aita, J. Appl. Phys. **101**, 123534 (2007)
72. S.M. Woodley, S. Hamad, J.A. Mejas, C.R.A. Catlow, J. Mater. Chem. **16**, 1927 (2006)
73. J. Kang, E.C. Lee, K.J. Chang, Phys. Rev. B **68**, 054106 (2003)
74. S. Wright, R.C. Barklie, J. Mater. Sci: Mater. Electron. **18**, 743 (2007)